Nanoporous Silver Thin Films: Multifunctional Platforms for Influencing Chain Morphology and Optical Properties of Conjugated Polymers

*Zeqing Shen and Deirdre M. O'Carroll**

Disordered nanoporous silver (NPAg) thin films fabricated by a thermally assisted dewetting method are employed as a platform to influence chain alignment, morphology, and optical properties of three well-known conjugated polymers. Grazing-incidence wide-angle X-ray scattering (GIWAXS) measurements show that the porous structure of the metal induces close π–π stacking of poly(3-hexylthiophene) (P3HT) chains and extended, planar chain conformations of poly(9,9-di-*n*-octylfluorenyl-2,7-diyl) (PFO) and poly[(9,9-di-*n*-octylfluorenyl-2,7-diyl)-*alt*-(benzo[2,1,3]thiadiazol-4,8-diyl)] (F8BT). A greater degree of vertically-oriented P3HT chains are found on NPAg compared with planar Ag. However, PFO and F8BT chain alignment is only affected when pore size is large. The optical properties of NPAg films are investigated by transmission and back-scattering spectroscopies. Strong back-scattering is observed for all NPAg morphologies, especially for NPAg with small pore sizes. Photoluminescence spectroscopy of conjugated polymer layers on NPAg showed pronounced emission enhancements (up to factors of 26) relative to layers on glass. The enhancements are attributed primarily to: 1) redistribution of conjugated polymer emission by Ag; 2) redirection of emission by polymer-filled nanopores; and 3) local electromagnetic field effects. This work demonstrates the potential of NPAg-thin films to influence molecular chain morphology and to improve light-extraction in organic optoelectronic devices.

1. Introduction

The influence of nanoscale confinement on organic conjugated polymer chain alignment and optical properties can greatly affect the overall performance of organic thin-film optoelectronic devices.[1–5] Although, numerous prior studies have characterized polymer chain alignment in bulk or planar thin-film environments,[6–10] the chain organization behavior of conjugated polymers on nanostructured surfaces has not been as widely studied.[5,11] X-ray and optical spectroscopy studies of the influence of nanoscale confinement on conjugated polymer chain alignment were carried out on nanoimprinted conjugated polymer films[4] and on conjugated polymer fibers formed within nanoporous dielectric templates.[12,13] In these studies, induced polymer chain alignment was observed and occurred in the direction normal to the confinement direction due to the flow of the polymer chains and the interaction between the polymer and the substrate/sidewall.[4]

Additionally, since conjugated polymer-based thin-film optoelectronics have lower device efficiencies compared with inorganic devices,[14] various optically-active nanostructures have been employed to manipulate light in thin conjugated polymer films due to the unique optical properties of nanostructures. Examples include: 1) patterned nonmetallic transparent substrates (patterned on either the outer surface[15] or inner surface[16] of the device), whereby the scattering properties of the patterned substrates were employed to improve light extraction efficiency from the light-emitting organic active layer; 2) addition of plasmonic nanostructures to take advantage of their light scattering and optical near-field properties.[17] Plasmonic nanostructures employed were either metallic nanoparticles/nanowires embedded into the devices' active layer and/or hole/electron transport layer,[18,19] or nanostructure arrays introduced onto the metallic electrodes.[20] In particular, nanohole arrays in metallic thin films have been used as both back electrodes[21] as well as front electrodes,[22,23] and showed improvements in light in-coupling or out-coupling, depending on the optoelectronic application. Most of the previous studies employing nanohole arrays were carried out on periodic arrays fabricated by nanoimprint lithography,[22] e-beam lithography[24] or focused-ion beam milling,[25] since the periodicity of the nanohole array played an important role in their plasmonic properties.[26] However, random nanoporous metal has also shown promising plasmonic and photonic properties,[27–30] and can be fabricated by large-area nonlithographic methods, such as dealloying.[31] Here, we develop a nonlithographic, thermally-assisted dewetting method to fabricate nanoporous silver (NPAg) films with different morphologies over areas >1 cm^2. We study the influence of NPAg on both the chain morphology

Z. Shen, Prof. D. M. O'Carroll
Department of Chemistry and Chemical Biology
Rutgers University
610 Taylor Road, Piscataway, NJ 08854, USA
E-mail: ocarroll@rutgers.edu
Prof. D. M. O'Carroll
Department of Materials Science and Engineering
Rutgers University
607 Taylor Road, Piscataway, NJ 08854, USA

DOI: 10.1002/adfm.201500456

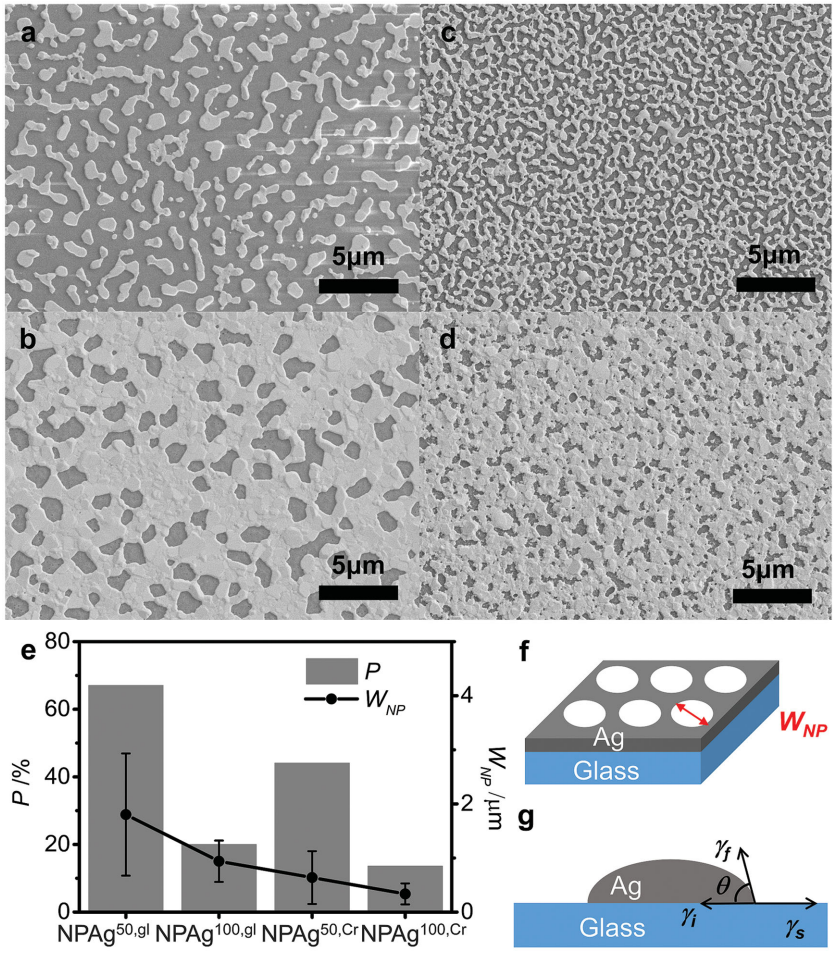

Figure 1. Representative SEM images of NPAg formed by thermal annealing: a) a 50-nm-thick Ag film on bare glass ($NPAg^{50,gl}$); b) a 100-nm-thick Ag film on bare glass ($NPAg^{100,gl}$); c) a 50-nm-thick Ag film on Cr-coated glass ($NPAg^{50,Cr}$); d) a 100-nm-thick Ag film on Cr-coated glass ($NPAg^{100,Cr}$) (samples from Batch 2; see the Experimental Section). Thermal annealing was carried out at ≈380 °C for 25 min for (a,c,d) and 5 min for (b). e) Porosities and pore widths of the different NPAg sample types shown in (a–d). f) Schematic of a NPAg film and definition of pore width, W_{NP}. g) Schematic of proposed Ag film dewetting mechanism that resulted in NPAg formation during thermal annealing. γ_f: surface energy of metal film, γ_i: surface energy at the interface of metal and substrate, γ_s: surface energy of bare substrate and θ: contact angle between silver surface and silver-substrate interface.

and optical properties of three different conjugated polymers of relevance to organic optoelectronics.

2. Results and Discussion

2.1. Morphology of Nanoporous Silver Films

Scanning electron microscopy (SEM) was employed to study the structure of NPAg fabricated by the dewetting method (**Figure 1**). In Figure 1a–d, the lighter regions are the Ag surface and the darker regions are the surface of the substrate. Typically, for a Ag film with a thickness of 50 nm on a glass substrate, after annealing at ≈380 °C for 25 min (see Experimental Section), the sample exhibited a Ag island structure (Figure 1a) with a significant separation between adjacent Ag islands and high porosity (ratio of bare substrate surface area to the total surface area). A Ag film with a thickness of 100 nm on a glass substrate formed a porous structure with large pore width but relatively low porosity after annealing for 5–10 min at ≈380 °C (Figure 1b); see Experimental Section and Table S1 (Supporting Information). Figure 1c shows the structure of Ag (50 nm initial thickness) on a Cr (5 nm) coated glass substrate after applying the same annealing conditions as for the 50-nm-thick Ag film on bare glass. Narrow anisotropic pore shapes with high porosity were formed in the Ag film. A 100-nm-thick Ag on Cr (5 nm)-coated glass resulted in porous structure (Figure 1d) with smaller pore width and porosity than for the 50-nm-thick Ag on Cr-coated glass case under the same annealing conditions. Shorter annealing times were typically employed for the 100-nm-thick Ag on glass sample (5–10 min) compared with those for the rest of the samples (25 min) to obtain discrete pore structures rather than Ag island structures.

In the remainder of the paper, we denote the silver film initial thickness and substrate type used for NPAg formation using the following notation: $NPAg^{t,sub}$, where t is the thickness of the silver film before the anneal, and *sub* is the substrate surface type (gl: glass; Cr: Cr coated glass). To quantitatively compare the structural differences between the four samples, average pore width, W_{NP}, and porosity, P, information were obtained by analyzing the SEM images using ImageJ software (Figure 1e,f and see Supporting Information).[32] $NPAg^{50,gl}$ had the largest W_{NP} of value 1.80 ± 1.13 μm, followed by $NPAg^{100,gl}$ with W_{NP} of 0.94 ± 0.38 μm, $NPAg^{50,Cr}$ (W_{NP} = 0.64 ± 0.49 μm); and $NPAg^{100,Cr}$(W_{NP} = 0.34 ± 0.19 μm). From this data, it was apparent that both the substrate type and initial Ag film thickness affected W_{NP}. Among samples underwent same annealing conditions (i.e. $NPAg^{50,gl}$, $NPAg^{50,Cr}$ and $NPAg^{100,Cr}$), the Ag films on bare glass had larger W_{NP} values than the Ag films on Cr-coated glass, and for samples with the same substrate surface, 50-nm-thick Ag films resulted in larger W_{NP} than the 100-nm-thick Ag films. The sequence of samples with P values from largest to smallest is as follows: $NPAg^{50,gl}$ (P = 67.05%); $NPAg^{50,Cr}$ (P = 44.08%); $NPAg^{100,gl}$(P = 19.99%); and $NPAg^{100,Cr}$(P = 13.58%). Therefore, after same annealing, 50-nm-thick Ag films resulted in higher P values than 100-nm-thick Ag films, and bare glass substrate samples had higher P values than Cr-coated glass substrate samples for samples with the same initial Ag thickness. This data implied that W_{NP} and P increased with decreasing initial Ag film thickness. Addition of the Cr adhesion layer decreased W_{NP} and P, but apparently affected W_{NP} more significantly than P. In addition, atomic force microscopy (AFM) characterization of the NPAg indicated that the thickness of the metal regions increased after

the dewetting process and the increase was related to the extent of dewetting. As a result, the final thicknesses of the Ag regions in the NPAg were approximately 75, 110, 120, and 160 nm for $NPAg^{50,Cr}$, $NPAg^{100,Cr}$, $NPAg^{100,gl}$, and $NPAg^{50,gl}$, respectively (see Figure S1, Supporting Information).

We hypothesize that the formation of the pores (Figure 1g) occurred because the surface energies in the thermally evaporated thin Ag film-on-substrate system were not in equilibrium.[33] When high temperature was applied to the film, the Ag atoms could "move" more easily[33] and the film reached equilibrium quickly. According to the Young–Laplace Equation, a system is in equilibrium when

$$\gamma_s = \gamma_i + \gamma_f \cdot \cos\theta \quad (1)$$

Only when the surface energy of the bare substrate, γ_s, is larger or equal to the sum of the surface energy of the metal film, γ_f, and the substrate-metal interface energy, γ_i, can the contact angle, θ, be 0°, in which case, the metal remains as a continuous flat film on the substrate. However, the surface energy of silver (≈1000 mJ m^{-2})[34] was larger than that of the substrate (glass surface energy: typically 250–500 mJ m^{-2}).[35] Therefore, to reach equilibrium, the contact angle increased and pores were formed. For the cases with a Cr adhesion layer between the Ag film and the glass substrate, the larger surface energy of Cr (≈2200 mJ m^{-2})[34] compared with Ag made the Ag prefer to "spread" on the Cr surface during the thermal anneal. Additionally, because Cr has a very strong affinity for oxygen, it was possible that an intermediate chromium oxide layer was formed at certain interface regions between Cr and the SiO_2 glass substrate, which made the Cr layer very difficult to move[36] on the substrate and further slowed down the dewetting of Ag. It was also possible that the Cr layer on the glass substrate was discontinuous (due to its thinness) and allowed small pores to form even with the presence of Cr. Overall, the Cr adhesion layer lead to smaller porosity compared with the analogous case without the Cr layer for the same thermal treatment conditions. Therefore, from this data, it was apparent that NPAg with different morphologies could be realized using the dewetting method by controlling the initial metal film thickness and the adhesion layer. Our work showed the annealing temperature and time also played a role in the final morphology of the metal film. The P and W_{NP} both appeared to increase as annealing time was increased. The stages at which nucleation and growth of the pores occurred likely depended in a more complex way on heating/cooling rate, temperature and time and requires further study beyond the scope of this paper.[37] In this study, a temperature was chosen such that the dewetting was observed within a time frame of a few minutes. Some variability was observed between different batches of samples fabricated at different times (see Experimental Section and Figure S2, Supporting Information), however, the trends in pore width, porosity and morphology discussed above were generally consistent.

2.2. GIWAXS Study of Polymer Chain Alignment

To investigate the influence of nanoporous metal on conjugated polymer thin film chain alignment and nanoscale morphology, GIWAXS measurements of three different well-known conjugated polymer materials drop-cast on NPAg were carried out and compared with measurements of drop-cast polymer films on planar surfaces. The three conjugated polymers employed were poly(3-hexylthiophene-2,5-diyl) (P3HT), poly(9,9-di-*n*-octylfluorenyl-2,7-diyl) (PFO) and poly[(9,9-di-*n*-octylfluorenyl-2,7-diyl)-*alt*-(benzo[2,1,3]thiadiazol-4,8-diyl)] (F8BT). As shown in **Figure 2**, the three conjugated polymers have significantly different molecular structures and conformations. For each polymer segment with 9 repeat units, after minimizing steric energy (using the MM2 force field method provided by Chem & Bio 3D software), a single P3HT chain had an almost perfectly planar molecular conformation (Figure 2a), while a single F8BT chain exhibited a twisted nonplanar conformation (Figure 2c). A single PFO chain had a conformation that exhibited a degree of planarity that was intermediate between that of P3HT and F8BT (Figure 2b). The molecular conformations of PFO and F8BT chains in the solid state, however, were expected to be slightly more planar than those depicted in Figure 2b,c considering the possible formation of intermolecular π–π interaction that can planarize the aromatic rings[38] and the existence of local environmental stresses.[39] In-plane (Figure 2d–f) and out-of-plane (Figure 2g–i) GIWAXS 1D line profiles of polymer thin films (≈80-nm thick) drop cast on both planar Ag and NPAg ($NPAg^{50,Cr}$) were extracted from 2D GIWAXS profiles; see Experimental Section and Figure S3 (Supporting Information). Notable differences in peak positions (d-spacings) and relative intensities (degree of order) were observed between planar Ag cases and NPAg cases for each polymer. Additionally, in **Figure 3** we show the influence of different NPAg on in-plane polymer chain alignment (Figure 3a–c) together with schematics representing the influence of NPAg relative to planar Ag (Figure 3d–g).

In the P3HT cases (Figure 2d,g), a clear peak shift between planar Ag and NPAg cases was observed only in the in-plane profiles. The shifting of the (020) peak, which corresponds to a π–π stacking X-ray reflection peak of P3HT,[40a] from q = 1.63 $Å^{-1}$ (d = 3.85 Å) for the planar Ag case to 1.65 $Å^{-1}$ (d = 3.81 Å) for $NPAg^{50,Cr}$ indicated that the P3HT π–π stacking was more closely packed in the NPAg sample.[40b] The other NPAg samples exhibited q values similar to or greater than that for the planar Ag substrate cases (1.62 $Å^{-1}$ for $NPAg^{50,gl}$, 1.64 $Å^{-1}$ for $NPAg^{100,Cr}$, and 1.65 $Å^{-1}$ for $NPAg^{100,gl}$); see Figure 3a and Supporting Information. The shifts in the position of the (020) peak for the NPAg samples can be explained by considering both W_{NP} and P—smaller W_{NP} and larger P correlated with larger q values, indicating more P3HT regions exhibited closer π–π stacking. Here, we hypothesize that the closer π–π stacking in the NPAg case was due to improved ordering of the polymer chains in the pores arising from flow induced ordering[41] or slower solvent evaporation times[40b] compared with the planar case.

Given that the (020) reflection peak was not apparent in the out-of-plane profiles, it was concluded that most of the P3HT chains packed with an edge-on or vertical configuration rather than face-on (see Figure 2d, inset).[4] Besides the (020) reflection peak, (100) and (300) reflection peaks that corresponded to the side chain distance could also be observed in the in-plane profiles. However, these peaks were much more dominant (higher in intensity) in the out-of-plane profiles, which proved

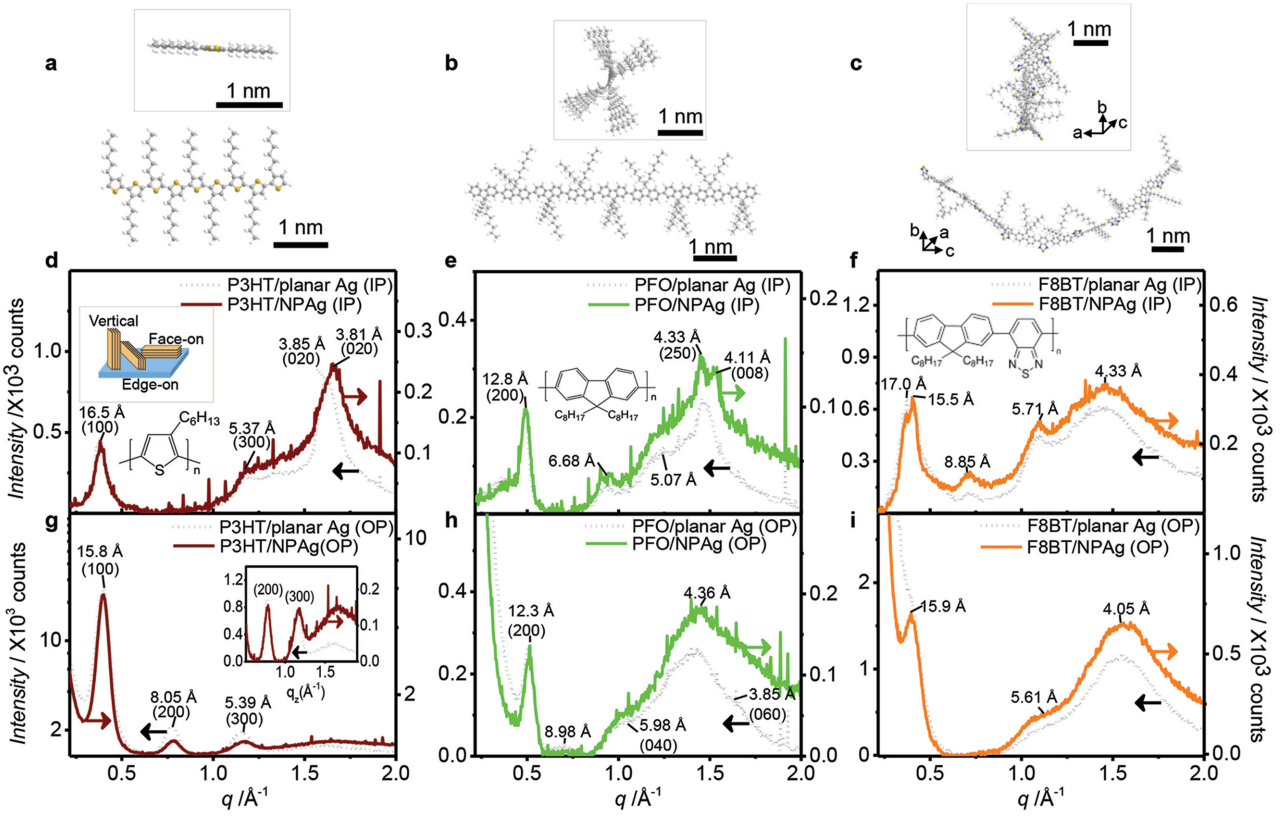

Figure 2. GIWAXS characterization of different conjugated polymers thin films on both planar and nanoporous Ag. 3D structure of a) P3HT, b) PFO, and c) F8BT molecular segments with 9 monomor repeat units after minimizing steric energy, viewed along (top panels) and perpendicular to (bottom) the polymer main chain axis. 1D in-plane GIWAXS profiles of d) P3HT, e) PFO, and f) F8BT drop cast on planar Ag (dots) and NPAg (solid colors). Inset in d): Schematic of vertical, edge-on and face-on polymer chain conformations and molecular structure of the monomer repeat unit of P3HT. Insets in e,f): Molecular structure of the monomer repeat unit of PFO and F8BT, respectively. 1D out-of-plane GIWAXS profiles of g) P3HT, h) PFO, and i) F8BT drop cast on planar Ag (dots) and NPAg (solid colors).

that most of the P3HT was packed with an edge-on configuration, with only a small portion of P3HT packed in the vertical configuration. By comparing the ratio of the in-plane (100) peak center intensity (I_{in}) to the out-of-plane (100) peak center intensity (I_{out}) in both planar and NPAg^{50,Cr} samples, we found that I_{in}/I_{out} increased from 1/52 for planar Ag to 1/38 for NPAg^{50,Cr}. This suggests that more P3HT chains with a vertical orientation were formed in the NPAg sample than on planar Ag.[4,42] The I_{in}/I_{out} ratios for the (100) peak for all of the other P3HT on NPAg samples were also larger than those for planar samples (Figure S5, Supporting Information). The induced vertically-packed P3HT chains were attributed to the interaction between P3HT and the surface of the pore walls,[43] see Supporting Information for details. Since the P3HT chains prefer to pack with their main chain axis parallel to the substrate surface (edge-on for planar substrates), the additional vertical substrate surface (inner wall surface of the nanopores) in the NPAg sample could, in effect, cause some of the P3HT chains to pack with their main chain oriented vertically. To summarize, on the planar Ag substrates, most of the P3HT polymer chains were aligned with edge-on configuration with π–π stacking distance, d_1. While on NPAg, a portion of P3HT in the pores packed into a vertical configuration from edge-on, and the P3HT in the pores packed with a smaller π–π stacking distance, d_2 (Figure 3d).

For PFO (Figure 2e,h), the broad backgrounds at $q \approx 0.4$ Å^{-1} and at $q \approx 1.4$ Å^{-1} in both in-plane and out-of-plane profiles were interpreted as scattering from PFO's disordered amorphous or glassy phase and β-phase chain conformations.[42,44,45] The strong and narrow peak with d-spacing ≈12.5 Å that can be observed in both in-plane and out-of-plane profiles was believed to correspond to the side chain distance between adjacent interchain-ordered PFO chains ((200) reflection peak).[44a,46] A very distinct peak splitting was observed at a relatively large q value only in the in-plane profiles of the NPAg samples which was absent for PFO on the planar substrates. Instead of a single peak (assigned to the (250) reflection)[42,45] at $q \approx 1.5$ Å^{-1} in the planar Ag in-plane profile, another peak (assigned to the (008) reflection)[42,45] was also observed in the NPAg in-plane profile. The (008) peak is believed to be a reflection peak associated with the polymer backbone (i.e., main-chain) axis.[44] The emergence of the (008) peak in the in-plane direction for the NPAg could be explained by the presence of more planar PFO main chains (i.e., the PFO β-phase chain conformation).[44,47] Here, we propose that stress applied to the polymer chains when they flow into the nanopores and during subsequent solvent

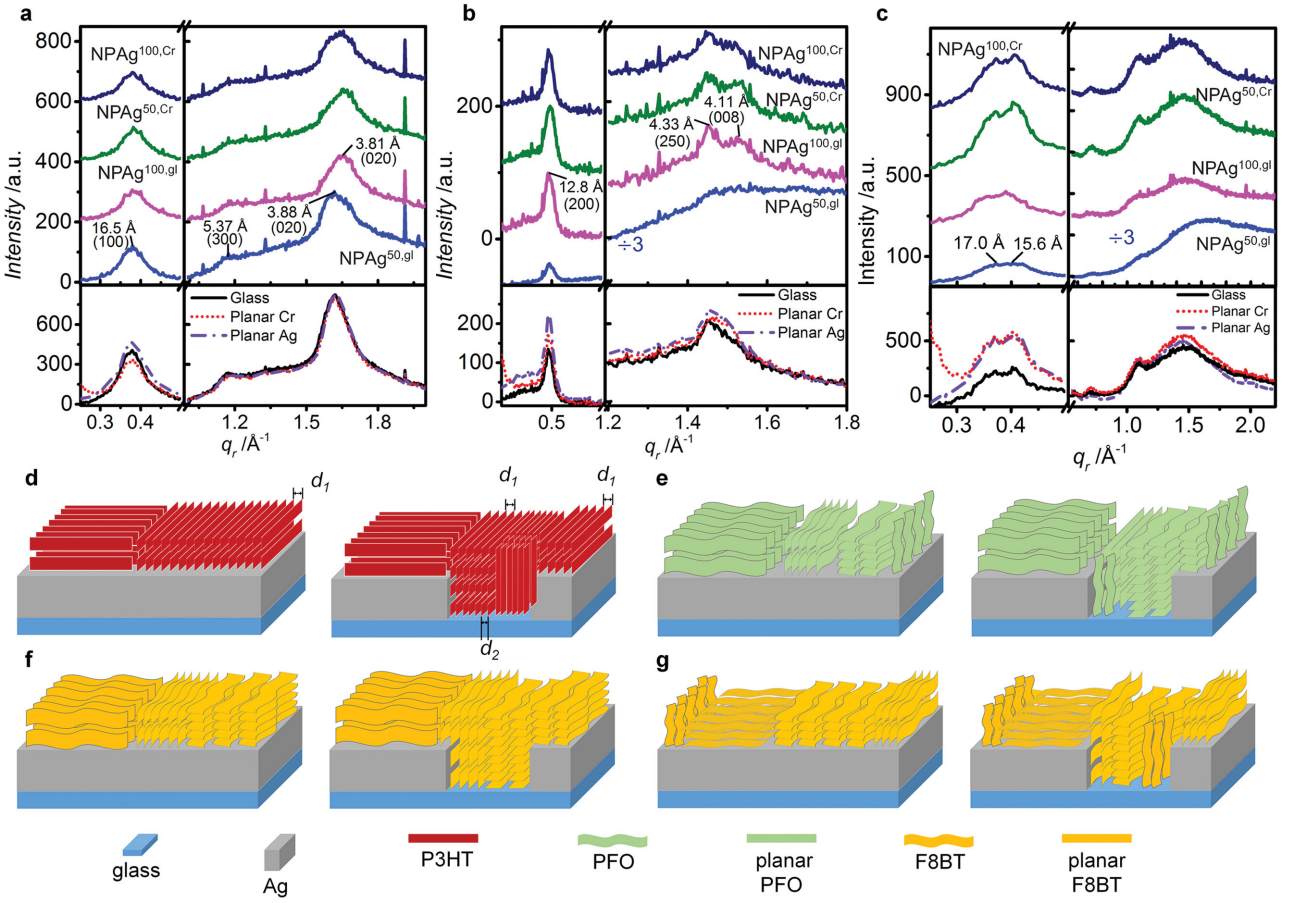

Figure 3. Influence of NPAg on polymer chain alignment. 1D in-plane GIWAXS profiles of a) P3HT, b) PFO, and c) F8BT drop cast on different NPAg substrates (top panels) and on planar Ag, planar Cr and glass substrates (bottom panels). The profiles acquired from samples with NPAg substrates in the top panels were offset in intensity for clarity. d) P3HT, e) PFO, and f,g) F8BT chain alignment schematics on planar Ag (left) and NPAg (right). The schematics are idealized in that they ignore amorphous chains and they only show the most representative ordered chain morphologies in a given sample. d_1 and d_2 are π–π stacking distances of P3HT on planar Ag and in the pores, respectively.

evaporation would facilitate the PFO planarization process and thus increase the fraction of the β-phase.[48] For the different NPAg cases, the apparent relative intensity of the (008) reflection peak compared with the (250) peak was most intense in the NPAg^{50,Cr} case and the relative intensity was lower for both the NPAg^{100,gl} and the NPAg^{100,Cr} cases (Figure 3b). This suggest that nanopores with smaller W_{NP} and larger P would facilitate the chain planarization process better and result in more β-phase PFO backbones; see Supporting Information.

Gaussian peak fitting was applied to the planar Ag and NPAg samples' in-plane and out-of-plane profiles (see Figure S6, Supporting Information). Results showed that, for the (200) peak, I_{in}/I_{out} for PFO on NPAg and on the planar samples were less than a value of 1 (Figure S7h, Supporting Information). This indicated that, there were more PFO chains aligned with side chains perpendicular to the substrates (i.e., edge-on chain configurations) than those with side chains aligned parallel to the substrate (face-on or vertical). The PFO-coated substrates in order of decreasing (200) I_{in}/I_{out} ratio are as follows: NPAg^{50,gl}, planar Ag, NPAg^{100,gl}, NPAg^{100,Cr}, NPAg^{50,Cr}, planar Cr, and glass (Figure S7, Supporting Information). This trend could be due to a combined influence of the pore structure and substrate surface. It seemed for PFO, the chain packing orientation was affected by the pore structure notably only when the pores were large, otherwise, the influence of the substrates dominated; see the Supporting Information. The schematics representing the PFO chain alignment on planar Ag case and NPAg are shown in Figure 3e. In both cases, there were more "edge-on" PFO chains than "face-on", and "vertical" chains. However, "face-on" and "vertical" chains could be induced when pores with a large enough size were employed. Moreover, for PFO on the NPAg, there was a comparatively larger amount of the more planar PFO β-phase chain conformation induced in the in-plane direction compared with that on planar surfaces.

For the F8BT cases (Figure 2f,i), a peak that was only observed in the in-plane profile occurred at 0.71 Å^{-1} (d-spacing of 8.85 Å). The relative intensity of this peak compared with the $d \approx 16.0$ Å peak for F8BT on all NPAg samples were larger than that for F8BT on the planar Ag sample (Figure 3c, see detailed discussion in the Supporting Information). Gaussian peak fitting was applied to separate the peak with $d \approx 16.0$ Å from the background scattering (see Figure S8, Supporting Information). I_{in}/I_{out} of this peak was then calculated for F8BT on different substrates. To explain the corresponding polymer chain alignment differences

between the planar Ag and NPAg cases, peak assignments must be made. There are currently two different opinions in the existing literature on the origin of F8BT X-ray reflections (see details in the Supporting Information).[49,50] According to the F8BT X-ray reflection peak assignments proposed by G. C. Faria et al. (see discussion in the Supporting Information), schematics Figure 3f were prepared. The results indicated that on both the planar Ag and NPAg, no F8BT chains had a vertical conformation. In both the planar Ag and NPAg samples, there were more F8BT chains with an edge-on configuration than a face-on configuration. When the pores were large and/or deep, more of the face-on chain configuration could be induced. Additionally, it was expected that the F8BT chains in the pores had a more planar main chain backbone. However, if the reflection peak assignments proposed by C. L. Donley et al. are applied, the results indicate that there were more F8BT chains with a face-on configuration than a vertical or edge-on configuration in both planar Ag and NPAg samples. When larger and/or deeper pores were present, the amount of F8BT chains with vertical and edge-on configuration could be increased (Figure 3g).

2.3. Optical Characterization

2.3.1. Light Scattering Properties of Nanoporous Silver Films

Dark-field reflection (i.e., back-scattering) images (under Xe lamp illumination) and dark-field reflection spectra were acquired prior to studying the optical properties of polymer-coated NPAg film systems (**Figure 4**). Figure 4a shows dark-field reflection images of the various samples. The dark-field images of glass and planar Ag were almost black in appearance, indicating a lack of back-scattering due to their planar structure. In contrast, for the NPAg samples, the dark-field images were significantly brighter due to strong back-scattering of the incident light by the nanostructures. The green–yellow color of the back-scattering suggested that the surface plasmons supported by the nanostructured silver arose from regions with relatively large dimensions and anisotropic shapes.[51] Similar scattering intensity trends were apparent in both the dark-field reflection images and spectra (Figure 4b). The scattering intensity was most intense for $NPAg^{100,Cr}$ and $NPAg^{50,Cr}$ and

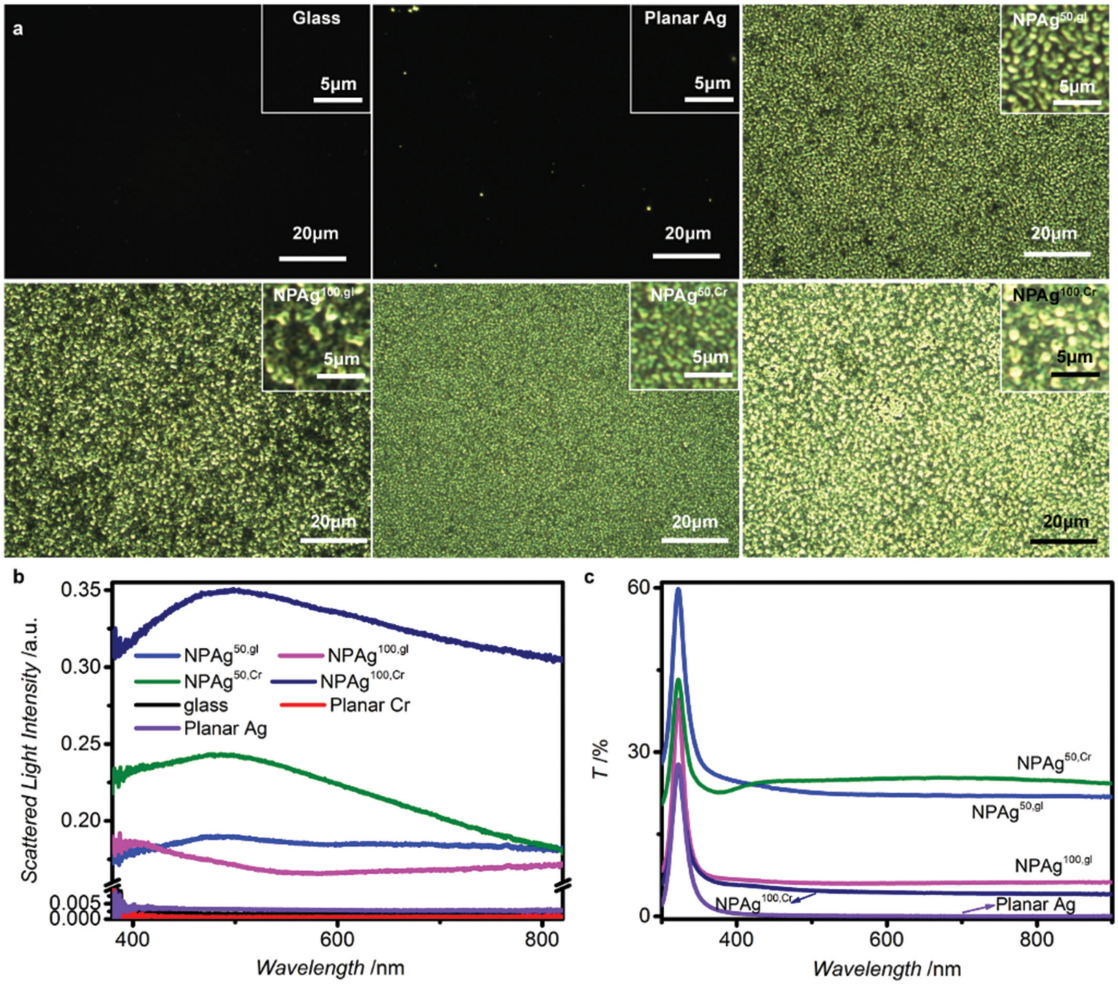

Figure 4. Optical characterization of bare NPAg films. a) Dark-field scattering images; b) dark-field scattering spectra; and c) transmission spectra of different NPAg films. All dark-field spectra showed above were an average of 5 spectra that were acquired under 0.02 s exposure time with 10 accumulations from different regions of one sample. The dark-field images were taken with an exposure time of 70 ms and had the same illumination intensity for all of the samples. Insets in a: zoomed in dark-field images of the different samples.

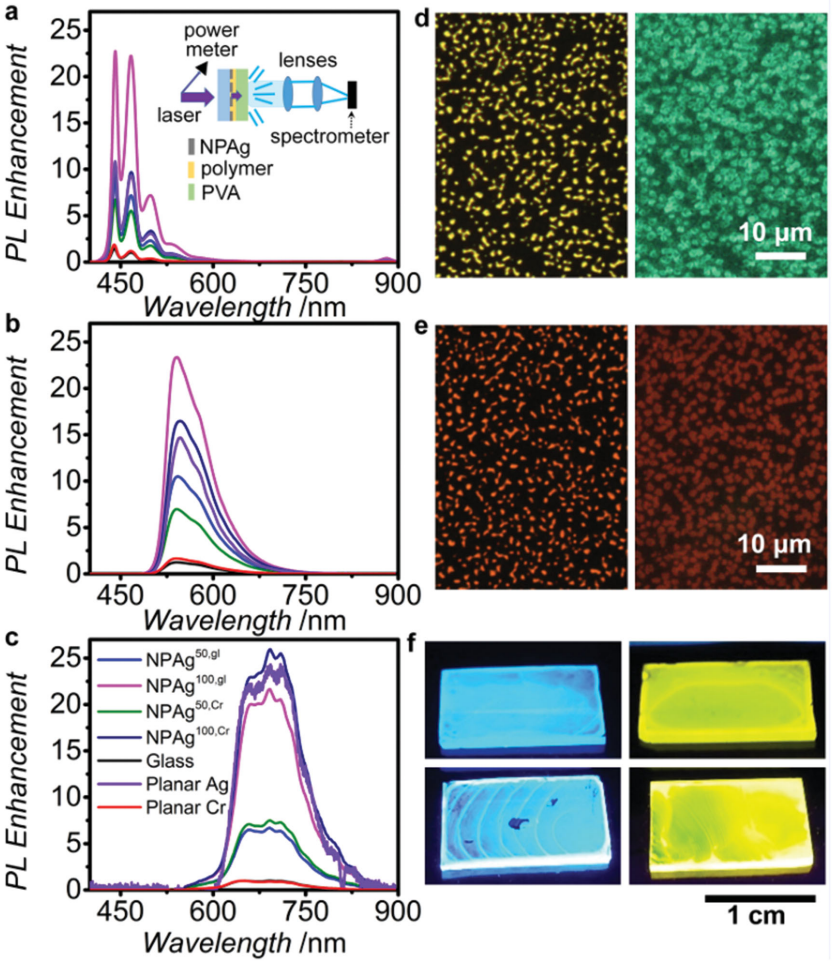

Figure 5. PL properties of conjugated polymers on different NPAg films. a) PL enhancement spectra of PFO on different NPAg relative to the PL intensity of PFO at 468 nm on glass; b) PL enhancement spectra of F8BT on different NPAg relative to the PL intensity of F8BT at 574 nm on glass; and c) PL enhancement spectra of P3HT on different NPAg relative to the PL intensity of P3HT at 693 nm on glass. The spectra were averaged from 72 different regions over the whole sample on different substrates. All of the spectra were excited through the glass substrate and collected from the polymer side of the sample. Inset in (a) is the schematic of PL experimental configuration. d,e) Correlated transmitted-light, bright-field image (left) and transmitted PL image (right) of PFO and P3HT, respectively, coated on $NPAg^{100,gl}$. f) Photographs of PFO (left) and F8BT (right)-coated $NPAg^{100,gl}$ (top) and planar Ag (bottom) substrates (1.5 cm × 1 cm) placed on UV lamp with polymer side facing up.

the $NPAg^{50,gl}$ and $NPAg^{100,gl}$ exhibited weaker scattering intensities. The reason for the back-scattering intensity trend can be explained by comparing W_{NP} and P. The nanopores with smaller W_{NP} scatter light more strongly than those with larger W_{NP}, and samples with larger P had a greater number of scattering sites. Also, the roughness of the Ag-covered region of the samples likely contributed to the scattering properties, particularly for $NPAg^{100,Cr}$ and $NPAg^{100,gl}$ due to the lower porosities (see Figure S10, Supporting Information). Broadband scattering arising from localized surface plasmon resonances (LSPRs) of anisotropic, randomly-organized nanostructures and out-coupled surface plasmon polaritons (SPPs) in the 400–800 nm wavelength range could account for the offset of the baseline intensity from 0 for each NPAg film spectrum.[52–54]

The two NPAg films with smallest W_{NP}, $NPAg^{50,Cr}$ and $NPAg^{100,Cr}$, had more broadband scattering. In addition to the broadband scattering, all NPAg film dark-field spectra showed scattering peaks in the ≈400–550 nm wavelength range most likely due to LSPRs associated with both the nanopores and the rough Ag surface regions. For the $NPAg^{50,gl}$, a very distinct peak was centered at 489 nm, likely due to the transverse LSPR of the nanoparticle structures and another peak occurred at ≈650 nm (see normalized spectra in Figure S11, Supporting Information) and was attributed to longitudinal LSPRs of the anisotropic nanoparticles.[55] In addition, a notable increase in long wavelength scattering (600–800 nm) was observed for the $NPAg^{100,gl}$ possibly due to out-coupled SPP modes.[56]

2.3.2. Transmittance Spectroscopy of Nanoporous Silver Films

Figure 4c shows the transmittance spectra of the various samples, with transmittance peaks at 320 nm observed for all of the Ag-containing samples due to the transparency of Ag near its plasma frequency. The overall transmittance, T, of different NPAg films inversely correlated with the volume of metal: larger metal volume resulted in a greater optical density. Between 300–400 nm, the transmittance peak intensity followed the trend in the P of different NPAg. The $NPAg^{50,gl}$ had the strongest peak, followed by $NPAg^{50,Cr}$, $NPAg^{100,gl}$, and $NPAg^{100,Cr}$. However, in the wavelength range from 400 to 900 nm, $NPAg^{50,Cr}$ had the highest transmittance of ≈25%, followed by $NPAg^{50,gl}$ (T ≈ 22%), $NPAg^{100,gl}$ (T ≈ 6%) and $NPAg^{100,Cr}$ (T ≈ 4%), with planar Ag (thickness of 100 nm) approaching $T = 0$. The reason why $NPAg^{50,Cr}$ had higher T than $NPAg^{50,gl}$ at the longer wavelength range remains unclear, but is possibly due to plasmonic properties of the structure of $NPAg^{50,Cr}$ such as out-coupling of SPPs or stronger local-field effects due to the smaller W_{NP}. No extraordinary optical transmission peaks were observed because of the lack of periodicity of the pore structure.[57]

2.3.3. Photoluminescence from Polymer-Coated Nanoporous Silver Films

Photoluminescence (PL) spectra of all polymer-coated samples were acquired and processed to investigate the influence of different NPAg on the emissive properties of polymer/NPAg systems (**Figure 5**). The absorbance spectra of the different

Table 1. PL enhancement of PFO, F8BT, and P3HT on different substrates relative to on glass at the specified emission wavelength (λ).

Substrate type	Photoluminescence enhancement [E_{PL}]		
	PFO [λ = 468 nm]	F8BT [λ = 574 nm]	P3HT [λ = 693 nm]
$NPAg^{100,Cr}$	9.6 ± 4.0	13.5 ± 6.5	25.9 ± 8.4
$NPAg^{100,gl}$	21.9 ± 9.1	17.6 ± 6.2	21.6 ± 4.8
$NPAg^{50,Cr}$	5.5 ± 2.4	5.5 ± 2.9	7.5 ± 1.5
$NPAg^{50,gl}$	7.1 ± 2.6	8.4 ± 3.6	6.7 ± 2.5
Planar Ag	9.3 ± 3.7	11.3 ± 6.3	24.3 ± 9.6
Cr	1.2 ± 0.6	1.3 ± 0.7	0.9 ± 0.2
glass	1.0 ± 0.3	1.0 ± 0.3	1.0 ± 0.1

polymer coatings on glass are shown in Figure S12, (Supporting Information).

The PL enhancement, $E_{PL}(\lambda_{em})$, at a particular PL emission wavelength (λ_{em}) was calculated as follows

$$E_{PL}(\lambda_{em}) = \frac{I_{PL}(\lambda_{em})}{I_{LP}(\lambda_{ex}) \times I_{PL,glass}(\lambda_{em})} \quad (2)$$

where $I_{PL}(\lambda_{em})$ is the PL intensity at the particular PL emission wavelength acquired from a given polymer-coated sample, $I_{LP}(\lambda_{ex})$ is the incident light power factor (see the Experimental Section) and $I_{PL,glass}(\lambda_{em})$ is the PL intensity at the particular PL emission wavelength acquired from polymer coated bare glass. Figure 5a–c shows averaged PL enhancement spectra of PFO, F8BT, and P3HT, respectively and Figure 5d,e shows correlated transmitted-light, bright-field, and transmitted PL microscopy images of PFO- and P3HT-coated NPAg, respectively. **Table 1** shows the averaged PL enhancement values for the polymer-coated planar Ag, Cr, and NPAg substrates relative to polymer-coated bare glass obtained at wavelengths corresponding to the $S_1 \rightarrow S_0$ 0–1 singlet exciton transition of the respective conjugated polymer (i.e., 468 nm for PFO, 574 nm for F8BT and 693 nm for P3HT).[58] This 0–1 peak was chosen for analysis to minimize contributions from reabsorption to the PL enhancement calculations.

2.3.3.1. Redistribution of Emission by Ag: For Cr(5 nm)-coated glass, polymer PL enhancements were negligible compared with the respective cases on bare glass, therefore, it was assumed that the presence of Cr contributed little to the PL enhancements. For the polymer-coated planar Ag film (100-nm-thick) on glass samples, PL enhancements relative to polymer on glass samples were significant ranging from 9.3 ± 3.7 and 11.3 ± 6.3 for PFO and F8BT, respectively, to 24.3 ± 9.6 for P3HT. These enhancements were primarily attributed to redistribution of the emission profile of the polymer optical transition dipoles by the almost optically-thick metal so that very little dipole power was emitted into the glass and, instead, dipole power was preferentially emitted into the polymer/air (i.e., forward) side of the sample from which the PL spectra were measured (see Figure 5a, inset). For thinner, more-transparent planar Ag films, it was expected that more power would be emitted into the glass substrate and, therefore, less emission would be detected in the forward direction. As a result, the PL enhancement values for thinner Ag would likely be lower than those for the thicker Ag film cases. Local electric field intensity enhancements arising from the surface roughness of the thermally-evaporated Ag films may also have contributed to a lesser extent to the planar Ag enhancements.

The PL enhancement for P3HT on planar Ag was significantly higher than for PFO and F8BT. This may be because the Ag film was slightly more transparent at shorter wavelengths (T = 0.16% at 468 nm; T = 0.06% at 574 nm; and T = 0.02% at 693 nm). Hence, the aforementioned redistribution of the emission profile by the Ag was expected to contribute more to the measured PL signal for P3HT (which emits at the longer wavelength) due to reduced PL emission into the glass substrate. Additionally, for P3HT, where polymer chains (and, hence, optical transition dipoles) were oriented predominantly with an edge-on configuration, roughness introduced by the metal film could have facilitated greater forward emission from the polymer layer than the less edge-on oriented polymers (i.e., PFO and F8BT).

2.3.3.2. Redirection of Emission by Nanopores: For the coated NPAg samples, the NPAg films with lower volumes of metal (i.e., initial Ag thickness of 50 nm), did not exhibit PL enhancements as large as those for the NPAg films with greater volumes of metal, most likely because more power was emitted into the glass substrate and, therefore, less emission was detected in the forward direction. Since the PL enhancements for P3HT on $NPAg^{100,gl}$ and $NPAg^{100,Cr}$ were not significantly different from P3HT on planar Ag (100-nm-thick), the redistribution of emission by Ag was still the main contributor to the PL enhancement. However, for PFO and F8BT on $NPAg^{100,gl}$, the PL enhancements increased significantly to 21.9 ± 9.1 and 17.6 ± 6.2, respectively, compared with the PL enhancements for the same polymers on planar Ag (9.3 ± 3.7 and 11.3 ± 6.3, respectively). This was primarily attributed to the wave-guiding ability of the pores whereby the fraction of emitted PL intensity directed/guided into the forward direction (i.e., propagating towards the polymer side and normal to the plane of the substrate) was increased at wavelengths near the absorption edge of the polymer, where refractive index and PL quantum efficiency were high.[30] This effect is similar to the absorption-induced transmission effect observed on nanoporous metal infiltrated with absorber materials.[29,30] Dark-field back-scattered light spectra obtained from the PFO- and F8BT-coated NPAg support this effect. Prior to polymer coating, the $NPAg^{100,gl}$ substrate exhibited the lowest back scattering intensity, however, after polymer coating, the back-scattering at the absorption edge/emission wavelength of those polymers increased significantly (see Figure S13, Supporting Information). The addition of Cr (i.e., $NPAg^{100,Cr}$), which reduced pore width and porosity, resulted in a notable decrease in the PL enhancement for both F8BT and PFO. This was likely due to the reduced wave-guiding ability of the filled pores due to the smaller effective "waveguide" diameter and depth, and greater inter-pore coupling. It was possible that this out-of-plane waveguide effect also occurred for NPAg with smaller Ag volume because we observed a similar decrease in PL enhancement on going from PFO- and F8BT-coated $NPAg^{50,gl}$ to the corresponding $NPAg^{50,Cr}$ case.

2.3.3.3. Local Electromagnetic Field Effects: For P3HT, since there was not a substantial increase in PL enhancement with the

NPAg relative to the planar Ag case, the aforementioned waveguide effect was not expected to have contributed significantly to the PL emission of P3HT. This may be because: a) of the significant edge-on and vertical orientation of the P3HT chains (which are not favorable for coupling to out-of-plane guided modes in the nanopores); and b) of the longer wavelength P3HT emission (which is less likely to be confined by a waveguide than emission at shorter wavelengths). However, for NPAg with the same Ag volume, the sample with a Cr-adhesion layer increased the PL enhancement of P3HT (by 10%–20%, on average) more than the case without Cr. This suggested that local plasmonic near-fields contributed notably to the PL enhancement of P3HT since NPAg samples with Cr had the smallest pore widths and strongest scattering at the excitation and emission wavelengths of P3HT. P3HT was effected by the plasmonic properties of NPAg because P3HT is a low PL quantum efficiency material (1%–10%),[59] which can be strongly affected by increases in the local density of optical states and, hence, increases in radiative decay rate and quantum efficiency arising due to plasmonic near-fields.[60] Changes in local excitation and emission intensity due to local plasmonic near fields cannot be ruled out for PFO and F8BT but were expected to be less significant than the aforementioned waveguide effect of the pores because of the reduced scattering and increased transmission of NPAg near the excitation wavelength of 355 nm (Figure 4b,c) and the already high PL quantum efficiency of these materials.[61] The plasmonic/photonic mechanisms discussed above were consistent with photographs of the various polymer-coated substrates placed on a UV lamp (Figures 5f and S14, Supporting Information).

2.3.3.4. Effects of Polymer Morphology Changes Caused by NPAg: In addition, changes in polymer chain orientation and conformation induced by different NPAg may also have affected the emission enhancements. The induced PFO face-on chains (favorable for out-of-plane emission) and PFO β-phase (higher quantum efficiency PFO phase than glassy phase)[62] by the NPAg may also have contributed slightly to the PL enhancement. The vertical P3HT chains induced by the NPAg (Figure 3d) were not expected to significantly change the emission direction of P3HT as it would still be into the plane of the substrate.

3. Conclusion

We investigated the effect of nanoporous Ag substrates fabricated using a thermally-assisting dewetting method on both the chain morphology and organization, and optical properties of various well-known conjugated polymer materials in thin film format. A combination of both pore size and porosity influenced the chain morphology and organization, as determined using grazing-incidence wide-angle X-ray scattering. For both planar and nanoporous Ag substrates, the edge-on organization of P3HT was overwhelmingly dominant but the nanopores did cause an increase in the fraction of vertically orientation polymer chains and reduced the P3HT π–π stacking distance (better ordering) relative to P3HT on planar Ag. In particular, for smaller pore width and larger porosity, the aforementioned changes in polymer chain morphology due to the presence of the pores were most pronounced. For PFO, in both planar and nanoporous Ag cases there was a greater fraction of polymer chains with an edge-on organization than face-on and/or vertical. Significant in-plane orientation of the β-phase PFO chain conformation occurred due to the nanoporous Ag compared with planar Ag. Additionally, the presence of the nanopores with large enough pore size in Ag increased the fraction of face-on and vertically oriented PFO chains. For F8BT, the effect of the nanopores on chain organization was less noticeable; however, nanoporous Ag with large pore width and/or depth transferred some face-on or edge-on chains to an orthogonal chain orientation. It was not apparent from this study that the intrinsic chain conformation of different conjugated polymers played a significant role in the observed changes in chain alignment on nanoporous metal compared with that on planar metal films. However, there were indications that, for polymers with more twisted chains, larger and/or deeper pores were required to affect the polymer chain orientation.

The optical characteristics of bare and conjugated polymer-coated nanoporous Ag were investigated using a combination of transmission, dark-field reflection (i.e., back-scattering), extinction, and PL measurements. The transmittance of the nanoporous Ag films followed changes in Ag volume and porosity at shorter wavelengths—optically thinner and higher porosity Ag films resulted in greater transmittance. Dark-field spectroscopy revealed that, for bare nanoporous Ag, there was a significant increase in back-scattering intensity relative to planar Ag and bare glass substrates. The strength of the back-scattering from nanoporous Ag depended on both pore size and porosity–scattering tended to be more intense for smaller pores and larger porosities. The back-scattering intensity typically reached a maximum at green wavelengths ≈500 nm for nanoporous Ag samples. However, larger, more discrete pores showed stronger back-scattering at shorter wavelengths.

Significant PL emission enhancements (values up to 26) were measured for the conjugated polymer films on both planar and nanoporous Ag compared with bare glass. A variety of effects were at play in contributing to the degree of emission enhancement including: 1) redistribution of the emitted power into the forward direction due to the optically-thick metal film; 2) redirection of emission due to the waveguiding ability of polymer-filled pores; 3) local electric field enhancement effect; and 4) changes in polymer chain orientation and conformation induced by NPAg. While the redistribution of emission increased with the volume of silver, waveguiding effects were strong for larger pores and at shorter wavelengths, and local electric field effects appeared to be stronger for smaller pores widths. For the polymers with high PL quantum efficiency and shorter emission wavelengths (i.e., PFO and F8BT), the redistribution of emission power and waveguiding effects were the most dominant effects. While for the polymer with low PL quantum efficiency and longer emission wavelength (i.e., P3HT), redistribution of emission power by the metal was the most dominant effect, followed by the local electric field enhancement effect, while the waveguiding effect was not apparent. The apparent absence of the nanopore waveguiding effect for the P3HT case was attributed to the low relative

fraction of the face-on chain configuration in P3HT compared with PFO and F8BT. Moreover, emission at shorter wavelengths was more likely to be confined and guided by the nanopores and, thus, be enhanced by the waveguiding effect. The low quantum efficiency of P3HT meant it was more likely to be effected by local electric field enhancement.

In summary, the aforementioned observations indicate that by controlling the pore size and porosity of nanoporous metal, conjugated polymer morphology and optical properties can be influenced in ways not possible using planar substrates. This study demonstrates the great light-extraction potential of nanoporous Ag films, indicating that they are useful platforms for conjugated polymer-based photonics and optoelectronics. Finally, the dewetting method reported here is an alternative approach for the fabrication of nanoporous silver films over optoelectronic device-relevant areas.

4. Experimental Section

Materials: Silver shot (99.9%; Strem Chemicals, Inc.), Chromium powder (99%; Alfa Aesar), Poly[(9,9-di-*n*-octylfluorenyl-2,7-diyl)-*alt*-(benzo[2,1,3]thiadiazol-4,8-diyl)] (F8BT) (M_n = 16754, M_w/M_n = 1.57; Sigma-Aldrich Co. LLC.), Poly(9,9-di-*n*-octylfluorenyl-2,7-diyl) (PFO) (M_n = 29155, M_w/M_n = 2.16; Sigma-Aldrich Co. LLC.), Poly(3-hexylthiophene-2,5-diyl) (P3HT) (M_n = 24091, M_w/M_n = 2.2; Rieke Metals, Inc.).

Nanoporous Silver Film Fabrication: Silver films with thicknesses of 50 or 100 nm were thermally evaporated on either bare glass or Cr (5 nm)-coated glass substrates (with areas of at least 1 cm^2) in an Edwards Coating System E306A thermal evaporator at a rate of 0.1 nm s^{-1}. Al_2O_3-coated tungsten wire baskets were used to hold the silver source metal during thermal evaporation. Prior to silver film evaporation, the glass substrates were sonicated in a detergent water solution (Fisherbrand Sparkleen 1 Detergent, 0.5 wt%) for 10 mins and, subsequently, were immersed in an HCl (≈36% aqueous): EtOH mixture (1:1 volume ratio) for 15 mins. The substrates were then rinsed with deionized water (18 MΩ) and dried under an air-gun. After silver evaporation, samples were transferred to a hotplate in an Argon-atmosphere glovebox. The hotplate was turned on and set to a temperature at which the top surface of a glass substrate was in the range 359–395 °C (see Table S1, Supporting Information). After a controlled period of time (5–25 min; Table S1, Supporting Information), the hotplate was turned off, and the samples were allowed to cool on the hotplate. In this study, three batches of NPAg samples were made at three different times (Batch 1, Batch 2, and Batch 3) and the pore width and porosity was determined from SEM images for each batch using ImageJ software; see the Supporting Information for further details.

GIWAXS Characterization: Grazing-incidence, wide-angle X-ray scattering (GIWAXS) measurements were acquired at the X9 beamline in Brookhaven National Laboratory (λ = 0.918 Å) to investigate the polymer chain alignment in different samples. For each sample, scattering patterns at 0.11° incident angles were acquired. Gaussian or Lorentzian peak fitting was applied to analyze the position and intensity of the characteristic diffraction peaks. To obtain conjugated polymer-coated NPAg for GIWAXS studies, F8BT (2 g L^{-1}), PFO (0.9 g L^{-1}) or P3HT (1 g L^{-1}) in chlorobenzene solution (50 µL) was drop cast onto the various NPAg samples (NPAg from Batch 1 and Batch 3 was employed for the F8BT-coated samples, and NPAg from Batch 2 and Batch 3 was employed for PFO- and P3HT-coated samples). Following coating of the NPAg with the polymer solution, samples were typically kept in a dark environment for 90 min and the solvent was allowed to evaporate. Subsequently, the samples were stored in an Argon-filled glovebox. For the GIWAXS data shown in Figures 2,3, NPAg samples from Batch 3 with F8BT coatings, and NPAg samples from Batch 2 with the PFO and P3HT coatings were employed. GIWAXS measurements were also acquired on polymer-coated glass, Cr(5 nm)/glass and Ag(100 nm)/glass samples for comparison with the polymer-coated NPAg samples. The 1D in-plane and out-of-plane GIWAXS line profiles shown in Figures 2,3 were plotted from data extracted from 2D GIWAXS profiles along lines rotated by 10° and 80° with respect to the expected horizontal q_r-axis of the 2D profiles using the view.gtk software developed at the X9 beamline,[63] respectively; see Figure S3 (Supporting Information). Due to the approximations we made in the data acquisition and processing (see the Supporting Information for details) the in-plane and out-of-plane line scans could not be used to quantify the percentage of each type of molecular conformation (e.g., edge-on, etc.) within the samples. However, the relative peak intensities (at a particular q value), shifts in peak positions, and I_{in}/I_{out} ratios allowed us to qualitatively assess the differences in molecular conformation between the various sample types.

Optical Characterization: For the optical measurements, conjugated polymer coatings were applied to the various sample substrates in the same way as that described above for the coated samples prepared for GIWAXS. Transmission spectra of bare NPAg films were collected using a S.I. Photonics Fiber Optic CCD Array UV–vis Spectrophotometer. Dark-field images and spectra of bare NPAg films and polymer-coated NPAg films were acquired with a Nikon Optiphot 66 optical microscope working in reflection mode and an Andor Shamrock SR 303i imaging spectrometer to investigate the scattering properties, in which a Xenon lamp was used as the light source. The PL emission properties of F8BT, PFO, and P3HT thin films on different substrates were investigated by exciting the film through the glass substrate with either the second or third harmonic of an AOT-YVO-25QSP/MOPA Q-witched pulsed Nd:YVO_4 laser (excitation wavelength of 355 nm for F8BT and PFO, and excitation wavelength of 532 nm for P3HT). PL spectra were collected from the polymer side (see Figure 5a, inset) using two achromatic doublet lenses in series and the Andor Shamrock SR 303i imaging spectrometer. Considering the differences of laser transmittance for different substrates, incident light power factors (ILP factors) were applied to the raw PL spectra of the polymers on different substrates to achieve the actual PL enhancements. ILP was calculated according to the following equation

$$\mathrm{ILP}(\lambda_{ex}) = \frac{T_{NPAg}(\lambda_{ex})}{T_{glass}(\lambda_{ex})} \quad (3)$$

where $T_{NPAg}(\lambda_{ex})$ is the transmitted laser power measured at the laser excitation wavelength (λ_{ex} = 355/532 nm) by integrating the spectrum of the laser acquired after the bare NPAg films and $T_{glass}(\lambda_{ex})$ is transmitted laser power at the laser excitation wavelength measured by integrating the spectrum of the laser acquired after bare glass. The ILP factors calculated at 355 and 532 nm laser excitation wavelengths matched very well with the transmittance values at 355 and 532 nm from the transmission spectra of NPAg (see Figure S15, Supporting Information). For the samples in Batch 3 (F8BT-, PFO- and P3HT-coated) 72 spectra were collected across the entire area of each sample and were analyzed and average as described in the main text. Transmitted-light, bright-field images, and transmission-mode PL images of PFO- and P3HT-coated $NPAg^{100}_{glass}$ samples (Batch 3) were acquired with a Nikon Optiphot 66 optical microscope working in transmission mode with the sample illuminated/excited from the glass substrate side. For the transmitted-light, bright-field images, a Tungsten-Halogen lamp was employed to illuminate the sample and, for the transmission-mode PL images, laser diodes with wavelengths of 405 and 532 nm were used as excitation sources for PFO- and P3HT-coated samples, respectively.

Supporting Information

Supporting Information is available from the Wiley Online Library or from the author.

Acknowledgements

Research was carried out in part at the Center for Functional Nanomaterials, Brookhaven National Laboratory, which is supported by the U.S. Department of Energy, Office of Basic Energy Sciences, under Contract No. DE-SC0012704 (Proposal No. 32195: Designing Plasmonic Electrodes for Inverted Organic Photovoltaics). This work was also supported in part through funding provided by the National Science Foundation (Grant No. DMR-1309459). The authors thank Dr. Kevin Yager and Christopher Petoukhoff for GIWAXS training and discussions.

Received: February 3, 2015
Revised: March 26, 2015
Published online: April 17, 2015

[1] S. Kappaun, C. Slugovc, E. J. W. List, *Int. J. Mol. Sci.* **2008**, *9*, 1527.
[2] D. M. O'Carroll, C. E. Petoukhoff, J. Kohl, B. Yu, C. M. Carter, S. Goodman, *Polym. Chem.* **2013**, *4*, 5181.
[3] N. Espinosa, M. Hösel, D. Angmo, F. C. Krebs, *Energy Environ. Sci.* **2012**, *5*, 5117.
[4] M. Aryal, K. Trivedi, W. Hu, *ACS Nano* **2009**, *3*, 3085.
[5] K. Shin, S. Obukhov, J. T. Chen, J. Huh, Y. Hwang, S. Mok, P. Dobriyal, P. Thiyagarajin, T. P. Russell, *Nat. Mater.* **2007**, *6*, 961.
[6] J. M. Geary, J. W. Goodby, A. R. Kmetz, J. S. Patel, *J. Appl. Phys.* **1987**, *62*, 4100.
[7] A. Salleo, R. J. Kline, D. M. DeLongchamp, M. L. Chabinyc, *Adv. Mater.* **2010**, *22*, 3812.
[8] C. W. Frank, V. Rao, M. M. Despotopoulou, R. F. W. Pease, W. D. Hinsberg, R. D. Miller, J. F. Rabolt, *Science* **1996**, *273*, 912.
[9] P. K. -H. Ho, L. Chua, M. Dipankar, X. Gao, D. Qi, A. T.-S. Wee, J. Chang, R. H. Friend, *Adv. Mater.* **2007**, *19*, 215.
[10] M. L. Chabinyc, M. F. Toney, R. J. Kline, I. McCulloch, M. Heeney, *J. Am. Chem. Soc.* **2007**, *129*, 3226.
[11] P. de Gennes, *Advances in Polymer Science*, Vol. *138*, Springer-Verlag, Berlin Heidelberg **1999**.
[12] S. Moynihan, P. Lovera, D. O'Carroll, D. Iacopino, G. Redmond, *Adv. Mater.* **2008**, *20*, 2497.
[13] K. Lo, R. Ho, Y. Liao, C. Hsu, F. Massuyeau, Y. Zhao, S. Lefrant, J. Duvail, *Adv. Funct. Mater.* **2011**, *21*, 2719.
[14] M. A. Green, K. Emery, Y. Hishikawa, W. Warta, E. D. Dunlop, *Prog. Photovolt.: Res. Appl.* **2012**, *20*, 12.
[15] D. Han, J. Kim, S. Na, S. Kin, K. Lee, B. Kim, S. Park, *IEEE Photonics Technol. Lett.* **2006**, *18*, 1406.
[16] J. Shin, D. Cho, J. Moon, C. W. Joo, S. K. Park, J. Lee, J. Han, N. S. Cho, J. Hwang, J. W. Huh, H. Y. Chu, J. Lee, *Org. Electron.* **2014**, *15*, 196.
[17] H. A. Atwater, A. Polman, *Nat. Mater* **2010**, *9*, 205.
[18] E. Stratakis, E. Kymakis, *Mater. Today* **2013**, *16*, 133.
[19] a) S. Chen, C. Yen, C. Yu, P. Kao, C. Lin, *Plasmonics* **2015**,*10*, 257; b) J. H. Park, Y. T. Lim, O. O. Park, J. K. Kim, J. Yu, Y. C. Kim, *Chem. Mater.* **2004**, *16*, 688.
[20] C. E. Petoukhoff, Z. Shen, M. Jain, A. Chang, D. M. O'Carroll, *J. Photonics Energy* **2015**, *5*, 057002.
[21] W. Bai, Q , Gan, G. Song, L. Chen, Z. Kafafi, F. Bartoli, *Opt. Express* **2010**, *18*, A620.
[22] S. Y. Chou, W. Ding, *Opt. Express* **2013**, *21*, A60.
[23] W. Ding, Y. Wang, H. Chen, S. Y. Chou, *Adv. Funct. Mater.* **2014**, *24*, 6329.
[24] K. Aydin, B. E. Ferry, R. M. Briggs, H. A. Atwater, *Nat. Commun.* **2011**, *2*, 517.
[25] Y. K. Kim, A. J. Danner, J. J. Raftery Jr., K. D. Choquette, *IEEE J. Sel. Top. Quantum Electron* **2005**, *11*, 1292.
[26] P. W. Flanigan, A. E. Ostfeld, N. G. Serrino, Z. Ye, E. Pacifici, *Opt. Express* **2013**, *21*, 2757.
[27] H. Chen, J. Long, Y. Lin, C. Weng, H. Lin, *J. Appl. Phys.* **2011**, *110*, 054302.
[28] J. Biener, G. W. Nyce, A. M. Hodge, M. M. Biener, A. V. Hamza, S. A. Maier, *Adv. Mater.* **2008**, *20*, 1211.
[29] J. A. Hutchison, D. M. O'Carroll, T. Schwartz, C. Genet, T. W. Ebbesen, *Angew. Chem.* **2011**, *123*, 2133; *Angew. Chem. Int. Ed.* **2011**, *50*, 2085.
[30] S. G. Rodrigo, F. J. García-Vidal, L. Martín-Moreno, *Phys. Rev. B: Condens. Mater. Phys.* **2013**, *88*, 155126.
[31] Z. Zhang, Y. Wang, Z. Qi, W. Zhang, J. Qin, J. Frenzel, *J. Phys. Chem. C* **2009**, *113*, 12629.
[32] Homepage of ImageJ software, http://imagej.nih.gov/ij/ (accessed: August, **2013**).
[33] C. V. Thompson, *Annu. Rev. Mater. Res.* **2012**, *42*, 399.
[34] a) H. Jones, *Mater. Sci. Technol.* **1971**, *5*, 15; b) B. Medasani, Y. H. Park, I. Vasiliev, *Phys. Rev. B: Condens. Matter Mater. Phys.* **2007**, *75*, 235436; c) L. Vitos, A. V. Ruban, H. L. Skriver, J. Kollár, *Surf. Sci.* **1998**, *411*, 186.
[35] A. J. Kinloch, *Adhesion and Adhesives-Science and Technology*, Chapman and Hall, London **1987**.
[36] P. Benjamin, C. Weaver, *Proc. R. Soc. London, Ser. A* **1961**, *261*, 516.
[37] J. Bischof, D. Scherer, S. Herminghaus, P. Leiderer, *Phys. Rev. Lett.* **1996**, *77*, 1536.
[38] U. Scherf, D. Neher, *Advances in Polymer Science*, Vol. *212*, Springer-Verlag, Berlin Heidelberg **2008**.
[39] S. Guha, M. Chandrasekhar, *Phys. Status Solidi B* **2004**, *241*, 3318.
[40] a) C. Muller, M. Aghamohammadi, S. Himmelberger, P. Sonar, M. Garriga, A. Salleo, M. Campoy-Quiles, *Adv. Funct. Mater.* **2013**, *23*, 2368; b) M. He, J. Ge, M. Fang, F. Qiu, Y. Yang, *Polymer* **2010**, *51*, 2236.
[41] H. D. Rowland, W. P. King, J. B. Pethica, G. L. W. Cross, *Science* **2008**, *322*, 720.
[42] C. Lee, S. Lai, W. Su, H. Chen, C. Chung, J. Chen, *J. Phys. Chem. C* **2013**, *117*, 20387.
[43] K. Yamamoto, S. Ochiai, X. Wang, Y. Uchida, K. Kojima, A. Ohashi, T. Mizutani, *Thin Solid Films* **2008**, *516*, 2695.
[44] a) S. H. Chen, H. L. Chou, A. C. Su, S. A. Chen, *Macromolecules* **2004**, *37*, 6833; b) M. Brinkmann, *Macromolecules* **2007**, *40*, 7532.
[45] C. H. Su, U. Jeng, S. H. Chen, S. J. Lin, Y. Y. Ou, W.-T. Chuang, A. C. Su, *Macromolecules* **2008**, *41*, 7630.
[46] S. H. Chen, A. C. Su, S. A. Chen, *J. Phys. Chem. B* **2005**, *109*, 10067.
[47] W. Chunwaschirasiri, B. Tanto, D. L. Huber, M. J. Winokur, *Phys. Rev. Lett.* **2005**, *94*, 107402.
[48] D. O'Carroll, D. Iacopino, A. O'Riordan, P. Lovera, É. O'Connor, G. A. O'Brien, G. Redmond, *Adv. Mater.* **2008**, *20*, 42.
[49] a) G. C. Faria, E. R. deAzevedo, H. von Seggern, *Macromolecules* **2013**, *46*, 7865; b) G. C. Faria, T. S. Plivelic, R. F. Cossiello, A. A. Souza, T. D. Z. Atvars, I. L. Torriani, E. R. deAzevedo, *J. Phys. Chem. B* **2009**, *113*, 11403; c) C. Muller, M. Esmaeili, C. Riekel, D. W. Breiby, O. Inganas, *Polymer* **2013**, *54*, 805.
[50] C. L. Donley, J. Zaumseil, J. W. Andreasen, M. M. Nielsen, H. Sirringhaus, R. H. Friend, J. Kim, *J. Am. Chem. Soc.* **2005**, *127*, 12890.
[51] K. L. Kelly, E. Gornado, L. L. Zhao, G. C. Schatz, *J. Phys. Chem. B* **2003**, *107*, 668.
[52] S. Morawiec, M. J. Mendes, S. Mirabella, F. Simone, F. Priolo, I. Crupi, *Nanotechnology* **2013**, *24*, 265601.
[53] Y. Nishijima, L. Rosa, S. Juodkazis, *Opt. Express* **2012**, *20*, 11466.
[54] K. Li, F. Xiao, F. Lu, K. Alameh, A. Xu, *New J. Phys.* **2013**, *15*, 113040.
[55] S. Link, M. B. Mohanmed, M. A. El-Sayed, *J. Phys. Chem. B* **1999**, *103*, 3073.

[56] C. J. Yates, I. D. W. Samuel, P. L. Burn, S. Wedge, W. L. Barnes, *Appl. Phys. Lett* **2006**, *88*, 161105.
[57] a) K. J. Klein Koerkamp, S. Enoch, F. B. Segerink, N. F. van Hulst, L. Kuipers, *Phys. Rev. Lett.* **2004**, *92*, 183901; b) M. J. Kofke, D. H. Waldeck, Z. Fakhraai, S. Ip, G. C. Walker, *Appl. Phys. Lett.* **2009**, *94*, 023104.
[58] a) D. O'Carroll, I. Lieberwirth, G. Redmond, *Nat. Nanotechnol.* **2007**, *2*, 180; b) R. Xia, G. Heliotis, D. D. C. Bradley, *Appl. Phys. Lett.* **2003**, *82*, 3599; c) K. Kim, J. W. Lee, S. H. Lee, Y. B. Lee, E. H. Cho, H. S. Noh, S. G. Jo, J. Joo, *Org. Electron.* **2011**, *12*, 1695.
[59] N. C. Greenham, I. D. Samuel, G. R. Hayes, R. T. Phillips, Y. A. R. R. Kessener, S. C. Moratti, A. B. Holmes, R. H. Friend, *Chem. Phys. Lett.* **1995**, *241*, 89.
[60] D. M. O'Carroll, J. S. Fakonas, D. M. Callahan, M. Schierhorn, H. A. Atwater, *Adv. Mater.* **2012**, *24*, OP136.
[61] R. Xia, G. Heliotis, Y. Hou, D. D.C. Bradley, *Org. Electron.* **2003**, *4*, 165.
[62] K. Asada, T. Kobayashi, H. Naito, *Jpn. J. Appl. Phys.* **2006**, *45*, L247.
[63] L. Yang, *J. Synchrotron Rad.* **2013**, *20*, 211.